Predictive GNSS Signal-Quality–Driven Receiver Adaptation for Robust UAV Navigation

Akash Kumar Mandal[a], Krittika Choudhuri[b], Ashik Paul[c], Ajay K. Poddar[d], Ulrich L. Rohde[e], and Swades De[a]
[a]Department of Electrical Engineering and Bharti School of Telecommunication, IIT Delhi, New Delhi 110016, India
[b]Department of Computer Science and Engineering, MCKV Institute of Engineering, West Bengal 711204, India
[c]Institute of Radio Physics and Electronics, University of Calcutta, West Bengal 700009, India
[d]Synergy Microwave Corporation, Paterson, NJ 07504, USA
[e]Massachusetts Institute of Technology, MA, USA, and University of the Joint Forces, Munich, Germany

***Abstract*—UAV navigation depends on reliable global navigation satellite system (GNSS) positioning but degrades under scintillation, multipath, and geometry variations. Conventional receivers react only after degradation. This paper proposes a predictive GNSS receiver that forecasts key metrics (carrier-to-noise ratio, amplitude and phase scintillation) using a task-coupled partitioned ensemble regressor for robust joint modeling. A satellite-based augmentation system-aided refinement further improves reliability using integrity-monitored satellites without modifying phase / delay / frequency-locked loops. Experiments on real ionospheric scintillation monitoring receiver-data show near-unity accuracy, outperforming statistical and extended Kalman filter baselines. Predictive adaptation reduces positioning variance excursions and lowers loss-of-lock probability to $\sim 10^{-9}$, achieving nearly two orders-of-magnitude integrity improvement.**

***Index Terms*—Adaptive GNSS receiver, global navigation satellite systems (GNSS), GNSS signal quality, predictive signal quality estimation, satellite-based augmentation system (SBAS)**

I. INTRODUCTION

Uncrewed aerial vehicles (UAVs) depend on global navigation satellite systems (GNSS) for navigation, control, and coordination, particularly in autonomous flight, low-altitude operations, and swarm scenarios [1], [2]. GNSS assist in UAV positioning and provides a key input to flight control loops, sensor fusion, and cooperative behaviors. As a result, even short-term GNSS degradation can trigger loss of situational awareness, control instability, or collision [3]. The reliability of GNSS-based UAV navigation is governed by signal-quality metrics rather than nominal accuracy alone. These metrics deteriorate in low-altitude and urban UAV operations due to dynamic geometry and frequent line-of-sight (LoS) blockage.

A. *Prior Art and Motivation*

Foundational studies have established that amplitude scintillation index (ASI) and phase scintillation index (PSI) arise from common physical mechanisms and jointly impact GNSS receiver tracking [4]–[6]. Amplitude scintillation increases thermal-noise jitter, while phase scintillation perturbs carrier tracking, causing cycle slips, loss-of-lock (LoL), and effective carrier-to-noise ratio (CNR) degradation [7]. These effects are sequentially coupled within the receiver processing chain, implying a degradation progression in which amplitude fluctuations precede phase instability, reduced CNR, and eventual tracking failure. Despite this understanding, most monitoring and mitigation strategies treat signal metrics independently, limiting proactive anticipation of failures [8], [9].

Conventional UAV GNSS receivers therefore rely on reactive, threshold-based mechanisms [10], adding or removing satellites based on instantaneous CNR, lock indicators, or elevation masks, and recomputing navigation solutions after lock loss [11]. While adequate in benign conditions, this approach is poorly suited to dynamic UAV environments [12], where degradation evolves gradually with geometry and motion; by the time failure is detected, mitigation windows have passed, leading to abrupt errors or navigation loss [13]. Although learning-based methods have recently shown promise for scintillation detection and short-term prediction [14], most focus on isolated tasks such as ASI without modeling its dependency on PSI and CNR [15], limited to post-processing [16].

A key insight in UAV navigation is that mobility makes GNSS degradation partially predictable, offering short forecast window [17]. Conventional receivers ignore this structure and react only after threshold violations [10], whereas predictive modeling can exploit mobility trends for proactive mitigation before tracking failure. Although scintillation-performance relationships and learning-based prediction are known [18], they remain unintegrated into practical receiver control. This motivates a predictive GNSS receiver where ASI, PSI, and CNR are jointly forecast as a supervisory layer to proactively adapt tracking, satellite weighting, and sensor fusion, bridging signal modeling with robust real-time UAV operation.

B. *Contributions and Significance*

The key contributions of this work are as follows:

1) We propose a dependency-aware task-coupled predictive ensemble (TCPE) framework that jointly predicts ASI, PSI, and CNR by capturing their physical coupling for reliable signal degradation forecasting.
2) We introduce satellite-based augmentation system (SBAS)-aided refinement that selects the most relevant integrity-monitored satellite to stabilize and enhance predicted signal quality.
3) We design a closed-loop GNSS receiver where forecasted signal quality guides a supervisory layer to

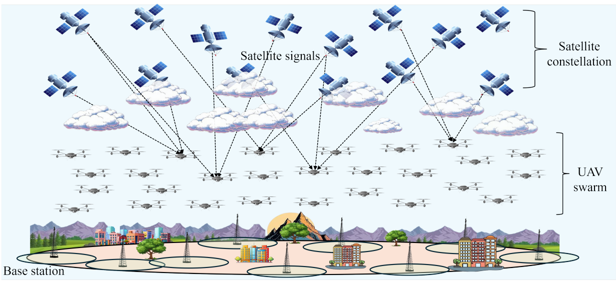

Fig. 1. System model depicting adaptive GNSS-receiver–aided UAV swarm.

proactively tune tracking while preserving conventional phase/delay/frequency (P/D/F) locked loops (LL).

The proposed receiver-integrated framework enables robust UAV navigation by mitigating GNSS degradation via early receiver-level adaptation, improving continuity and resilience without changes to existing GNSS infrastructure.

II. System Model

Consider a GNSS-enabled UAV swarm navigation (cf. Fig. 1), where multiple UAVs operate concurrently on satellite-based positioning. Each UAV is equipped with an onboard GNSS receiver that independently tracks signals from a visible subset of constellation satellites. The UAVs are assumed to fly at low to medium altitudes, where propagation is impacted by ionospheric irregularities, terrain- and building-induced multipath, and dynamic LoS variations due to mobility. Thus, the signal-quality metrics CNR, ASI, and PSI evolve over time exhibiting correlated behavior. In addition to GNSS satellites, the receiver is assumed to track SBAS satellites transmitting integrity-monitored signals from geostationary orbits. For each signal-quality metric, predicted values are refined by blending model outputs with SBAS-derived measurements, where the refinement operates purely at the data-processing level without requiring additional acquisition or tracking. The standard receiver front-end and tracking loops remain unchanged, while the proposed predictive models run at a slower supervisory time scale to inform higher-level receiver adaptation.

III. Predictive GNSS Receiver Architecture and Signal-Quality Modeling

For each satellite link tracked by a UAV GNSS receiver (identified by PRN), standard post-tracking signal-quality observables, CNR, ASI, and PSI, are estimated from conventional loop statistics. The receiver computes geometry parameters (AZM and ELV) and time metadata, including GPS week number and time-of-week. The feature vector is defined as: $x \triangleq$ [PRN, Week No, GPS TOW, AZM, ELV].

A. Modeling of GNSS Signal Quality: SBAS-aided TCPE

We define three interleaved models $\mathcal{F}$ on the historical data for initial value estimation of ASI, PSI, and CNR, denoted as a_s, ϕ_s, and γ_s, respectively. Mathematically:

$$\hat{a_s} = \mathcal{F}_{a_s}(x),\ \hat{\phi_s} = \mathcal{F}_{\phi_s}(x, \tilde{a_s}),\ \hat{\gamma_s} = \mathcal{F}_{\gamma_s}(x, \tilde{a_s}, \tilde{\phi_s}). \tag{1}$$

where $\tilde{(\cdot)}$ denotes the second-level value refinements using the SBAS-induced corrections attained as:

$$\begin{aligned} \tilde{a_s} &= \alpha_{a_s}\hat{a_s} + \sum_{\forall i \in \mathcal{S}} \beta_{a,i} a_i^{(\text{SBAS})} \\ \tilde{\phi_s} &= \alpha_{\phi_s}\hat{\phi_s} + \sum_{\forall i \in \mathcal{S}} \beta_{\phi,i} \phi_i^{(\text{SBAS})} \\ \tilde{\gamma_s} &= \alpha_{\gamma_s}\hat{\gamma_s} + \sum_{\forall i \in \mathcal{S}} \beta_{\gamma,i} \gamma_i^{(\text{SBAS})} \end{aligned} \tag{2}$$

where $a_i^{(\text{SBAS})}$, $\phi_i^{(\text{SBAS})}$, and $\gamma_i^{(\text{SBAS})}$ are the amplitude scintillation index, phase scintillation index, and CNR values for the SBAS satellites, respectively. $\mathcal{S}$ is the set of all SBAS satellites with the coefficients obeying unity norm condition: $\alpha + \sum_{\forall i \in \mathcal{S}} \beta_{j,i} = 1$, $j \in \mathcal{T}$, such that $\mathcal{T} \triangleq \{a_s, \phi_s, \gamma_s\}$. For modeling, we propose a novel TCPE regression, given as:

$$\hat{y} = \mathcal{F}(x; \boldsymbol{\Theta}) = \frac{1}{M} \sum_{i=1}^{M} g_m(x; \theta_m) \tag{3}$$

where $\boldsymbol{\Theta}_j = \{\theta_{m,j}\}_{m=1}^{M_j}$, $\boldsymbol{\Theta} = \{\boldsymbol{\Theta}_j\}_{j \in \mathcal{T}}$ with M_j and $\theta_{m,j}$ being the number of parameters and parameters of the mth base learner model for task j. The base learner g_m is a partitioned regression rule, defined as follows:

$$g_m(x; \theta_m) = \sum_{l=1}^{L_m} c_{m,l} 1\{x \in \mathcal{R}_{m,l}(\theta_m)\} \tag{4}$$

where $1\{\cdot\}$ is an indicator function, $c_{m,l} \in \mathbb{R}^3$ is the vector of predicted values for the three signals in $\mathcal{T}$, L_m is the number of terminal regions (leaf nodes) created by the mth base learner's recursive partition of the feature space, and $R_{m,l}(\theta_m)$ denotes the region l of the feature space induced by recursive partitions. The construction of each region is obtained by minimizing a multi-task impurity objective:

$$\mathcal{L}(\boldsymbol{\Theta}, \boldsymbol{\alpha}, \boldsymbol{\beta}) = \sum_{j \in \mathcal{T}} \frac{1}{L_{m,j}} \sum_{l=1}^{L_{m,j}} \sum_{x_n \in \mathcal{R}_{m,l}} w_j l(y_{j,n} - c_{m,l}) \tag{5}$$

where $\boldsymbol{\alpha} = [\alpha_{a_s}, \alpha_{\phi_s}, \alpha_{\gamma_s}]$, $\boldsymbol{\beta} = [\{\beta_{a_s,i}\}_{i \in \mathcal{S}}, \{\beta_{\phi_s,i}\}_{i \in \mathcal{S}}, \{\beta_{\gamma_s,i}\}_{i \in \mathcal{S}}]$, $l(z) = \frac{1}{2}z^2$ (or Huber loss), and w_j are the non-negative task-weights. We pose the SBAS-aided TCPE regressor training as a constrained empirical-risk minimization:

$$\begin{aligned} (\mathbf{P}1): &\quad \min_{\boldsymbol{\Theta}, \boldsymbol{\alpha}, \boldsymbol{\beta}} \ \mathcal{L}(\boldsymbol{\Theta}, \boldsymbol{\alpha}, \boldsymbol{\beta}) + \lambda \Omega(\boldsymbol{\Theta}) \\ \mathbf{C}11: &\quad \alpha_j + \sum_{\forall i \in \mathcal{S}} \beta_{j,i} = 1,\ \alpha_j, \beta_{j,i} > 0,\ \forall j \end{aligned} \tag{6}$$

where $\Omega(\boldsymbol{\Theta})$ penalizes tree complexity (e.g., total leaf count or cost-complexity pruning). $\mathbf{C}11$ enforces unity-norm constraint. To find α and β-values, we suggest three perspectives.

1) Closed-form calibration of global blend weights: If SBAS contributions are aggregated into a single per-sample reference, i.e., $s_{j,n} = \sum_{i \forall \mathcal{S}} \beta_{j,i} y_{j,n,i}^{(\text{SBAS})}$, such that $\sum_{i \forall \mathcal{S}} \beta_{j,i} = 1 - \mu_j$ and we parameterize $\tilde{y}_{j,n} = \mu_j \hat{y}_{j,n} + s_{j,n}$ with a global $\mu_j \in [0, 1]$. Then for squared loss, the optimal μ_j^* admits a projection of a closed-form:

$$\mu_j^* = \prod_{[0,1]} \frac{\sum_{n=1}^{N} (y_{j,n} - s_{j,n})(\hat{y}_{j,n} - s_{j,n})}{\sum_{n=1}^{N} (\hat{y}_{j,n} - s_{j,n})^2 + \varepsilon} \tag{7}$$

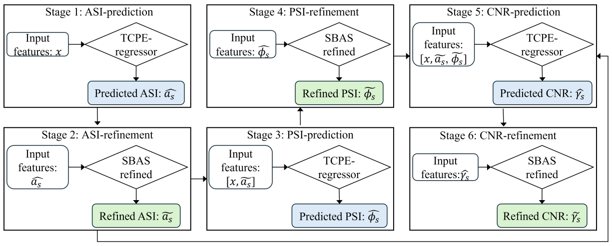

Fig. 2. SBAS-aided TCPE modeling of signal-quality metrics $\mathcal{T}$.

$\prod_{[0,1]}(z) = \min\{1, \max\{0, z\}\}$ and $\varepsilon \downarrow 0$ avoids division by 0.

2) Distance-aware weights (learnable kernel): For sample-wise (n) SBAS weights, let $d_{n,i} = \sqrt{(\mathrm{AZM}_n - \mathrm{AZM}_i^{(\mathrm{SBAS})})^2 + (\mathrm{ELV}_n - \mathrm{ELV}_i^{(\mathrm{SBAS})})^2}$ be the AZM/ELV angular distance to SBAS satellite i, s.t.:

$$\beta_{j,i}(x_n; \kappa_j) = \exp(-\kappa_j d_{n,i}) \Big(\sum_{k \in \mathcal{S}_n} \exp(-\kappa_j d_{n,k}) \Big)^{-1} \tag{8}$$

where κ_j is a learnable parameter which is tuned in the optimization process. This respects the "nearest-SBAS by AZM/ELV" heuristic but generalizes it into a trainable soft-nearest-neighbor using the following optimization formulation:

$$\begin{aligned} (\mathbf{P}2): &\quad \min_{\boldsymbol{\Theta}, \boldsymbol{\alpha}, \boldsymbol{\beta}} \; \mathcal{L}(\boldsymbol{\Theta}, \boldsymbol{\alpha}, \boldsymbol{\beta}) + \lambda \Omega(\boldsymbol{\Theta}) \\ \mathbf{C}21: &\quad \mu_j \in [0,1] \,, \gamma_j \geq 0 \end{aligned} \tag{9}$$

$(\mathbf{P}2)$ is solved via *alternating minimization*, with closed-form updates for the refinement weights and standard regularized training for the base predictor in (5) and (8), respectively.

3) Probably suboptimal solution: If instead a single α_j and $\beta_{j,i}$ can be used accross multiple samples, we solve:

$$\begin{aligned} (\mathbf{P}3): &\quad \min_{\alpha_j, \beta_{j,i}} \sum_n \Big(y_{j,n} - \alpha_j \hat{y}_{j,n} - \sum_{i \in \mathcal{S}_n} \beta_{j,i} y_{j,n,i}^{(\mathrm{SBAS})} \Big)^2 \\ \mathbf{C}31: &\quad \alpha_j + \sum_i \beta_{j,i} \leq 1, \; \alpha_j, \; \beta_{j,i} \geq 0 \end{aligned} \tag{10}$$

$(\mathbf{P}3)$ is a classical quadratic programing, which can be efficiently solved using QP-solvers to directly yield α_j and $\beta_{j,i}$.

Remark 1. *Only one SBAS reference is usually the most optimal way to obtain the least error solution of $\mathcal{T}$. In such a case, the PRN is obtained as: PRN$_{\mathrm{SBAS}} = \arg\min_{i \in \mathcal{S}} d_{n,i}$.*

A detailed architectural-flow is shown in Fig. 2.

B. Predictive GNSS Receiver Architecture

The predictive GNSS receiver design is shown in Fig. 3. The UAV-mounted antenna feeds the RF front-end, which performs amplification, filtering, down-conversion, and ADC. The baseband samples $r[k]$ are:

$$r[k] = A[k] c(kT_s - \tau[k]) e^{j(2\pi f_D[k] k T_s + \phi[k])} + n[k] \tag{11}$$

where $T_s = 1/f_s$, and $A[k], \tau[k], f_D[k], \phi[k], n[k]$ denote amplitude, code delay, Doppler, phase, and noise. Over each T_{int}, early, prompt, and late correlators $Z_E[k], Z_P[k], Z_L[k]$ are computed for tracking and signal-quality estimation. The DLL estimates $\tau[k]$ via: $e_{\mathrm{DLL}}[k] = |Z_E[k]| - |Z_L[k]|$, i.e.,

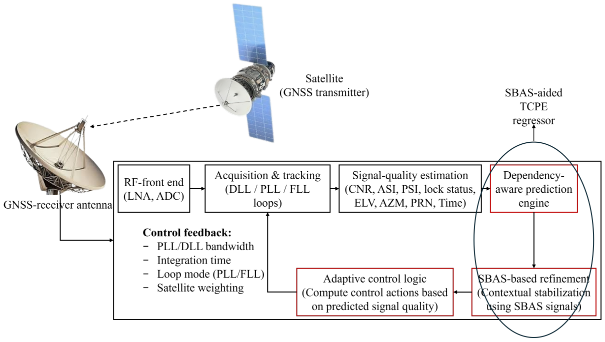

Fig. 3. Predictive GNSS receiver architecture.

$$\hat{\tau}[k+1] = \hat{\tau}[k] + K_{\mathrm{DLL}}(B_{\mathrm{DLL}}[k]) e_{\mathrm{DLL}}[k] \tag{12}$$

with gain $K_{\mathrm{DLL}}(\cdot)$ set by $B_{\mathrm{DLL}}[k]$. Carrier tracking (PLL/FLL-assisted PLL) uses: $e_{\mathrm{PLL}}[k] = \arg(Z_P[k])$, i.e.,

$$\begin{aligned} \hat{\phi}[k+1] =& \hat{\phi}[k] + \hat{f}_D[k] T_{\mathrm{int}} \\ \hat{f}_D[k+1] =& \hat{f}_D[k] + K_{\mathrm{PLL}}(B_{\mathrm{PLL}}[k]) e_{\mathrm{PLL}}[k] \end{aligned} \tag{13}$$

where $B_{\mathrm{PLL}}[k]$ is the carrier loop bandwidth. Defining $q_{\mathrm{trk}}[k] = [\hat{\tau}[k], \hat{\phi}[k], \hat{f}_D[k]]^T$ and $u_{\mathrm{trk}}[k] = [B_{\mathrm{DLL}}[k], B_{\mathrm{PLL}}[k]]^T$ with $q_{\mathrm{trk}} \in \mathcal{Q}, u_{\mathrm{trk}} \in \mathcal{U}$, we have:

$$q_{\mathrm{trk}}[k+1] = \mathbf{f}_d(q_{\mathrm{trk}}[k], Z_E[k], Z_P[k], Z_L[k], u_{\mathrm{trk}}[k]) \tag{14}$$

where $\mathbf{f}_d(\cdot)$ follows (12)–(13). From tracking, vectors $\mathcal{T}[k]$ and x are computed, and the *dependency-aware prediction engine* with *SBAS-based refinement* yields $\hat{\mathcal{T}}[k+1]$. The control is:

$$u_{\mathrm{trk}}[k] = \pi(\hat{\mathcal{T}}[k+1]) \tag{15}$$

where $\pi : \mathcal{T} \to \mathcal{U}$ maps signal-quality states to actions. This outer loop proactively tunes parameters (e.g., bandwidths, integration time, weighting) using predicted $\hat{\mathcal{T}}[k+1]$, via an offline look-up table. Performance evaluation is done next.

IV. RESULTS AND DISCUSSION

The results for the proposed GNSS receiver is shown in this section. The proposed modeling approach is contrasted with the state-of-the-art signal modeling approaches – **statistical modeling:** ARIMA, SARIMAX, EKF [19]; **learning-based modeling:** ϵ-SVR and DT [14] and the positioning performance of the predictive GNSS receiver architecture is contrasted to the conventional reactive GNSS receiver [10].

A. Key Performance Indicators (KPIs)

1) Root mean-squared error (RMSE): Let $\{y_i\}_{i=1}^N$ denote the true values and $\{\hat{y}_i\}_{i=1}^N$ the corresponding predicted values. The RMSE is defined as: $\mathrm{RMSE} = \sqrt{\frac{1}{N} \sum_{i=1}^N (y_i - \hat{y}_i)}$

2) Coefficient of determination (R^2): Let $\bar{y} = \frac{1}{N} \sum_{i=1}^N y_i$ denote the sample mean of the true values. The coefficient of determination is defined as: $R^2 = 1 - \frac{\sum_{i=1}^N (y_i - \hat{y}_i)^2}{\sum_{i=1}^N (y_i - \bar{y})^2}$.

TABLE I

AVERAGE GAIN IN R^2 ACCURACY METRIC WITH THE INCREASE IN THE NUMBER OF ESTIMATORS, M (AVERAGE R^2 AT $M = 50$ IS $\approx 95\%$)

Depth, L	Increment in the number of estimators, ΔM		
	From 50 to 100	From 100 to 200	From 200 to 300
5	1.12×10^{-3}	1.75×10^{-3}	-4.7×10^{-4}
10	1.14×10^{-3}	7.19×10^{-5}	-5.57×10^{-4}
20	1.54×10^{-3}	7.76×10^{-4}	-7.82×10^{-5}
30	1.73×10^{-3}	1.19×10^{-3}	2.78×10^{-4}
No limit	1.86×10^{-3}	9.69×10^{-4}	1.94×10^{-4}

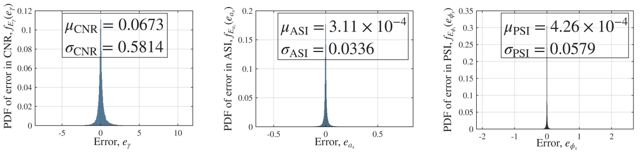

(a) PDF of error in CNR (b) PDF of error in ASI (c) PDF of error in PSI

Fig. 4. Distribution of errors in predicted GNSS signals, $(M, L) = (100, 20)$.

3) Average positioning accuracy: It is measured in terms of root-mean-square error $\sigma_{\text{pos}}^{(k)}$ for the kth epoch is given as:

$$\sigma_{\text{pos}}^{(k)} \approx \text{GDOP}\frac{c}{\sqrt{2}}\sqrt{\frac{1}{N}\sum_{i\in\nu[k]}^{N}\frac{B_{\text{DLL}}^{(i)}}{\gamma_i T_{\text{int}}^{(i)}}} \tag{16}$$

where GDOP is the geometric dilution of precision, c is the speed of light, and $\nu[k]$ is the set of satellites tracked in the navigation solution at epoch k (Refer Appendix for details).

4) LoL probability: $P_{\text{LoL}} = \frac{1}{K}\sum_{k=1}^{K} 1(\sigma_{\text{pos}} < \sigma_{\text{pos,th}})$.

B. Data Collection and Curation

The GNSS dataset, collected from ISMR files in April 2024, consists of 24-hr multi-satellite observations over L1, L2, and L5 bands, providing 67 signal, geometry, and ionospheric features (e.g., signal strength, scintillation, TEC, spectral, and lock-time metrics). Raw data were converted to `.csv` using `pandas`, with GPS week–TOW mapped to UTC for alignment. Missing samples were handled via interpolation and forward/backward filling, with severely corrupted entries removed. Features were preprocessed through geometric normalization, outlier mitigation (IQR and z-score), and engineering (cyclic TOW, one-hot PRN, week normalization). Finally, only L1 features were retained, and all files were merged into a time-synchronized dataset for evaluating the SBAS-aided TCPE framework with targets in $\mathcal{T}$.

C. Optimality of the Predictive Signal Modeling

From Table I, we note that although beyond the 95% gain attainable with 100 estimators, the increment with ΔM is insignificant, which optimizes for unlimited number of leaf nodes per estimator at 100 estimators. However, this would lead to significant computation overhead at no significant R^2 gains. Therefore, we choose the optimal hyperparameter set as $M = 100$ and $L = 20$, which leads to a limited runtime complexity and descent accuracy. For these settings, we analyze the following estimation error equation: $\hat{x} = x + e$, where $\hat{x}$ is the estimated value of the GNSS signal metric using the proposed estimation technique, x is the true value, and e is the estimation error. In Fig. 4, we study the probability density functions (PDF) for the error in CNR (e_γ), ASI (e_{a_s}), and PSI (e_{ϕ_s}). As notable from Fig. 4, PDF of the errors follow a Gaussian distribution with near zero mean and strict variance, which verifies that the proposed approach renders an unbiased and near-true estimates of GNSS signal quality metrics.

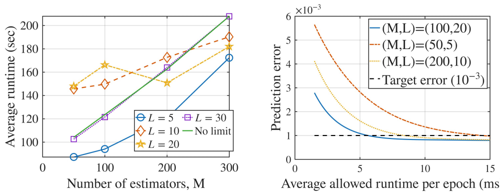

(a) (b)

Fig. 5. Complexity analysis of SBAS-aided TCPE signal estimation approach.

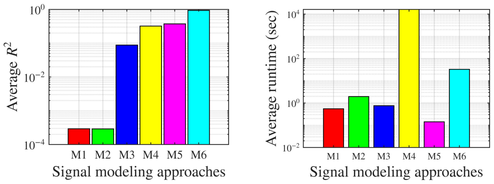

(a) (b)

Fig. 6. Comparative performance analysis of the proposed signal modeling approach with the state-of-the-art signal modeling approaches; M1: ARIMA, M2: SARIMAX, M3: EKF, M4: ϵ-SVR, M5: DT, M6: proposed.

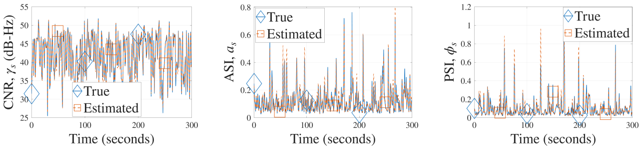

(a) (b) (c)

Fig. 7. Predictive GNSS signal estimation using proposed SBAS-aided TCPE.

D. Complexity of Proposed Predictive Modeling

The complexity of the proposed SBAS-aided TCPE regressor is primarily determined by the ensemble size M and the maximum number of leaf regions L per base learner. Since each learner predicts over L partitions, increasing M or L directly raises inference cost. Fig. 5(a) shows average runtime growing monotonically with M, with larger L causing steeper escalation; the "no limit" case illustrates the worst-case burden under unrestricted tree growth, motivating the complexity penalty $\Omega(\boldsymbol{\Theta})$ in (9). Fig. 5(b) highlights the accuracy–complexity tradeoff: prediction error decreases with runtime but saturates due to irreducible noise. Among the tested settings, (M, L)=$(100, 20)$ offers the best balance, reaching the target error 10^{-3} at much lower runtime than $(50, 5)$ and the higher-cost $(200, 10)$. Overall, TCPE enables controllable complexity via (M, L), supporting efficient deployment in latency-constrained predictive GNSS receivers.

E. Comparative Analysis of Predictive Signal Estimation

Fig. 6 shows the accuracy–complexity advantage of the proposed method M6 over state-of-the-art baselines. In Fig. 6(a),

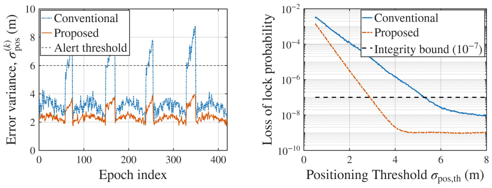

(a) Position error vs. runtime (b) P_{LoL} vs. $\sigma_{\mathtt{pos,th}}$

Fig. 8. Performance comparison of conventional vs. proposed GNSS receiver.

M1–M2 yield negligible fidelity with $R^2 \approx 3 \times 10^{-4}$, while M3 attains only $R^2 \approx 10^{-1}$ due to breakdown of its locally linearized Gaussian assumptions under nonlinear, nonstationary scintillation fades. M4 and M5 improve to $R^2 \approx 0.45$ and 0.55, whereas M6 achieves near-unity accuracy, i.e., nearly two orders-of-magnitude gain over M3 and more than three over M1–M2. Fig. 6(b) shows that M1 and M3 require ≈ 0.6–0.8 s, M2 incurs ≈ 2–3 s, and M4 is prohibitive with runtime $> 10^4$ s; M5 is lightweight (≈ 0.15–0.2 s) but less accurate. Importantly, M6 offers the best tradeoff, achieving $R^2 \approx 0.95$ with practical runtime of 30–50 s, i.e., 10^2–10^3 times faster than M4 while outperforming low-complexity baselines. Finally, Fig. 7 shows close overlap between estimated and true metrics using M6, with RMSE values of 8.2×10^{-2} (CNR), 6.8×10^{-4} (ASI), and 1.11×10^{-4} (PSI).

F. Performance of Predictive GNSS Receiver

Fig. 8 compares the proposed predictive GNSS receiver with the conventional reactive design [10]. In Fig. 8(a), the conventional receiver shows large fluctuations in positioning error variance $\sigma^{(k)}_{\text{pos}}$ (typically 3–4 m), with excursions beyond the 6 m alert limit and peaks of 7.5–9 m. In contrast, the proposed receiver remains within 2–3 m, with mild increases up to ~ 4 m and no threshold violations, achieving a 40%–50% variance reduction and eliminating critical spikes. Fig. 8(b) shows that the conventional receiver violates the 10^{-7} integrity bound [20] for $\sigma_{\text{pos,th}} \lesssim 5.5$ m, with $P_{\text{LOL}} \approx 10^{-4}$ at ~ 2 m and above 10^{-6} near 4 m. The proposed design decays faster, crossing below 10^{-7} at ~ 3 m and reaching $P_{\text{LOL}} \approx 10^{-9}$ for $\sigma_{\text{pos,th}} \geq 4$ m, about two orders-of-magnitude improvement.

V. CONCLUDING REMARKS

This paper presented a predictive GNSS receiver for UAVs that proactively mitigates scintillation-induced degradation. Unlike reactive designs, it employed dependency-aware forecasting to jointly model signal-quality metrics and anticipate degradation. SBAS-aided refinement improved robustness using integrity-monitored satellites without altering standard PLL/DLL/FLL loops. The resulting design operates as a low-rate supervisory layer, preserving compatibility while enabling data-driven adaptation, thereby improving positioning stability and reducing LoL in challenging ionospheric conditions.

ACKNOWLEDGEMENT

This work was supported in part by the Tehri Hydroelectric Development Corporation under Grant THDC/RKSH/R&D/F2076/1036; and in part by the Science and Engineering Board under Grant CRG/2023/005421.

APPENDIX

Position error covariance: $\mathbf{P}_x = (\mathbf{H}^T\mathbf{W}\mathbf{H})^{-1}$, where $\mathbf{H}$ is the geometry matrix, $\mathbf{W} = \operatorname{diag}(w_1, \cdots, w_N)$, such that $w_i = 1/\sigma^2_{\rho,i}$ is the inverse pseudorange variance (PV). PV satisfies: $\sigma^2_{\rho,i} \approx \frac{c^2}{2\gamma_i}\frac{B^{(i)}_{\text{DLL}}}{T^{(i)}_{\text{int}}}$. Thus, $\sigma_{\text{pos}} = \text{GDOP}\sqrt{\sum_{i=1}^{N} \sigma^2_{p,i}}$.

REFERENCES

[1] Y. Yang *et al.*, “UAV waypoint opportunistic navigation in GNSS-denied environments,” *IEEE Trans. Aerosp. Electron. Syst.*, vol. 58, no. 1, pp. 663–678, 2021.

[2] A. K. Mandal *et al.*, “A novel statistically-aided learning framework for precise localization of UAVs,” in *Proc. IEEE 97th VTC2023-Spring*, 2023, pp. 1–5.

[3] Z. Wu *et al.*, “A failure-resistant, lightweight, and tightly coupled GNSS/INS/vision vehicle integration for complex urban environments,” *IEEE Trans. Instrum. Meas.*, vol. 73, pp. 1–13, 2024.

[4] F. Tang *et al.*, “Drifting ionospheric scintillation simulation for L-band geosynchronous SAR,” *IEEE J. Sel. Top. Appl. Earth Obs. Rem. Sen.*, vol. 17, pp. 842–854, 2023.

[5] J. Liu *et al.*, “Residual-based fault detection and exclusion with enhanced localization integrity,” *IEEE Trans. Veh. Technol.*, vol. 72, no. 5, pp. 5798–5808, 2022.

[6] R. A. M. Lopes *et al.*, “Ionospheric scintillation mitigation with Kalman PLLs employing radial basis function networks,” *IEEE Trans. Aerosp. Electron. Syst.*, vol. 59, no. 5, pp. 6878–6893, 2023.

[7] B. Breitsch *et al.*, “GNSS carrier phase cycle slips due to diffractive ionosphere scintillation: Simulation and characterization,” *IEEE Trans. Aerosp. Electron. Syst.*, vol. 56, no. 5, pp. 3632–3644, 2020.

[8] M. Maaref *et al.*, “Aerial vehicle protection level reduction by fusing GNSS and terrestrial signals of opportunity,” *IEEE Trans. Intel. Transp. Syst.*, vol. 22, no. 9, pp. 5976–5993, 2021.

[9] Y. Sun *et al.*, “G5GIM: Integrity monitoring for GNSS/5G integrated navigation of urban vehicles,” *IEEE Trans. Instrum. Meas.*, vol. 72, pp. 1–13, 2023.

[10] Q. Zhou *et al.*, “Target localization for distributed hybrid active-passive radars,” *IEEE Trans. Aerosp. Electron. Syst.*, 2025.

[11] S. Ogutcu *et al.*, “Assessing the reliability of the GNSS loss of lock indicator (LLI) index for PPP across different types of GNSS receivers,” *Adv. Space Res.*, 2026.

[12] Y. Li *et al.*, “Cooperative elliptic positioning through single UAV during GNSS outages,” *IEEE Trans. Wirel. Commun.*, vol. 23, no. 10, pp. 12 749–12 764, 2024.

[13] I. Srisomboon *et al.*, “Positioning and navigation approaches using packet loss-based multilateration for UAVs in GPS-denied environments,” *IEEE Access*, vol. 12, pp. 13 355–13 369, 2024.

[14] A. Siemuri *et al.*, “A systematic review of machine learning techniques for GNSS use cases,” *IEEE Trans. Aerosp. Electron. Syst.*, vol. 58, no. 6, pp. 5043–5077, 2022.

[15] W. Xie *et al.*, “On the multi-GNSS real-time PPP time transfer assisted by predicted receiver clocks,” *Meas. Science Tech.*, vol. 36, no. 11, p. 116304, 2025.

[16] H. Chen *et al.*, “Deep learning based GNSS time series prediction in presence of color noise,” in *Pos. Nav. Mac. Learn. Met.* Springer, 2024, pp. 99–126.

[17] G. Nathan *et al.*, “Design and deployment of a hybrid neural network for real-time GPS correction in slow moving, low SWaP, UAV flight systems,” *GPS Sol.*, vol. 29, no. 3, pp. 1–25, 2025.

[18] J. R. van der Merwe *et al.*, “Optimal machine learning and signal processing synergies for low-resource GNSS interference classification,” *IEEE Trans. Aerosp. Electron. Syst.*, vol. 60, no. 3, pp. 2705–2721, 2024.

[19] H. Li *et al.*, “Deformation prediction modeling for levee structures based on environmental loads using SARIMAX and LSTM,” *Adv. Space Res.*, 2025.

[20] H. Jing *et al.*, “Integrity monitoring of GNSS/INS based positioning systems for autonomous vehicles: State-of-the-art and open challenges,” *IEEE Trans. Intel. Transp. Syst.*, vol. 23, no. 9, pp. 14 166–14 187, 2022.